Optimizing nanosheet nickel cobalt oxide as an anode material for bifunctional electrochemical energy storage and oxygen electrocatalysis

Sangeun Cho[a], Seongwoo Lee[a], Bo Hou[b], Jongmin Kim[a], Yongcheol Jo[a], Hyeonseok Woo[a], Sambhaji M. Pawar[a], Akbar I. Inamdar[a], Youngsin Park[c], SeungNam Cha[b], Hyungsang Kim[a, *], Hyunsik Im[a, *]

a Division of Physics and Semiconductor Science, Dongguk University, Seoul 04620, South Korea

b Department of Engineering Science, University of Oxford, Parks Road, OX1 3PJ, UK

c School of Natural Science, UNIST, Ulsan 44919, South Korea

E-mail addresses: hskim@dongguk.edu (H. Kim), hyunsik7@dongguk.edu (H. Im).

Abstract

Mesoporous Ni-Co oxide (NCO) nanosheet electrodes are fabricated on Ni foam via an electrodeposition technique. Their bifunctional activities for electrochemical energy storage and electro-catalysis for water splitting in strong alkaline media are optimized by varying the ratio of concentrations of the Ni and Co precursors. The ratio-based changes vary the pore size of the NCO nanosheets between 92.5 and 200 nm, and structural analyses reveal that the electrode films have a spinel $NiCo_2O_4$ structure. The obtained specific capacitance varies dramatically between 613 and 2704 Fg^{-1} at 2 mA cm^{-2}, with good capacity retention (80-90%) after 2000 cycles. The NCO nanosheet electrodes also exhibit a good oxygen evolution reaction at the surface. The lowest overpotential (315 mV at 10 mA cm^{-2}) is obtained with a Tafel slope of 59 mV dec^{-1}. The observed bifunctional activities of the new NCO nanosheet electrode are superior to those of nanostructured NCO electrodes prepared via hydrothermal and SILAR methods. The analyses regarding the electrochemically active surface area and electrochemical impedance spectroscopy, together with the observed electrochemical performance, reveal that the most-optimized Ni and Co composition produces the synergetic effects of an electrochemically active surface area and great stability.

1. Introduction

The global demand for energy has been increasing continuously and is expected to double within 15 years. However, traditional fossil fuel energy sources are limited and their heavy consumption has created serious environmental issues such as air pollution and global warming [1]. To fulfill the increasing energy demand with consideration of the environment and the limited availability of material resources, efficient and cost-effective energy conversion and storage devices which are combined with renewable energy sources have been devised and tested. Among the various devices, electrochemical supercapacitors and hydrogen generation from water splitting are promising because of their unique advantages and environmental friendliness. Although they use different mechanisms to generate and store energy, the core technological element they have in common is electrochemically efficient, active, durable electrodes fabricated using methods that are cheap.

The electrochemical supercapacitors and electrocatalysts now used for water splitting generally use strong alkaline media (typically potassium hydroxide: KOH) as electrolytes. Their performance is evaluated according to many factors they have in common such as electrochemically active surface area and the resistance at the electrode/electrolyte interface. These are evaluated using the same

techniques, and it is very useful to understand their performance by measuring bi-functionalities of the electrode. For electrocatalytic water splitting, the following two types of reactions occur: the oxygen evolution reaction (OER) at the anode and the hydrogenevolution reaction (HER) at the cathode [2]. For bifunctional electrodes, the electrocatalytic OER occurs in a higher potential region than with the electrochemical energy-storage process. In general, bifunctional devices typically operate within a wide window of potential.

Over the past few decades, metal hydroxides/oxides have been used as efficient OER and HER catalysts [3-8]. The first-row transition metal compounds have more active OER catalytic properties, compared with noble metal oxides, due to smaller d values and lower crystal-field activation energies [9,10]. Furthermore, the use of noble metal oxides is limited because of their high cost and rarity. Electrocatalytic and electrochemical activities are strongly dependent on electrical conductivity, morphology, and the number of active sites of the electrodes used. It has been demonstrated that nanostructured catalysts with large surface area and defect- induced active reaction sites significantly reduce OER over- potential (<300 mV) [11,12]. Recently, a number of catalysts based on iron (Fe), cobalt (Co), nickel (Ni), and zinc (Zn) hydroxides or oxides, have attracted much interest in terms of the OER and supercapacitor applications. This is because of their widespread abundance, low cost, high corrosive resistance in alkaline media, variable valence states, and environmental friendliness [13-16].

Among the various transition metal oxides, NieCo oxide (NCO)- based materials have attracted wide attention due to their low cost, environmental friendliness, and high theoretical capacity [17-19]. To improve electrochemical performance, it is important to design a material so that it can provide large surface area and high electrical conductivity. Bulk materials (in powder form) are structurally unstable and suffer from poor electrochemical performance due to their limited surface area, which determines the number of the active reaction sites [20-22]. A general strategy is to grow binder- free nanostructured active materials on mesoporous substrates [18,23,24]. The preparation of binder-free nanostructured electrode materials such as nanotubes, nanosheets, and nanowires could improve the electrochemically active surface area and electrical conductivity of their bulk forms, thereby enhancing their electro- catalytic and electrochemical properties. The direct growth of NCOs onto metal-foam substrates is especially advantageous because of their structural integrity, high aspect ratio, easy accessibility, and large number of active sites [25].

For this study, mesoporous NCO nanosheets were prepared on Ni foam via a binder-free electrodeposition technique that was followed by annealing. Well-defined mesoporous NCO nanosheets with different Ni-Co compositional ratios were obtained by varying the Ni and Co precursor concentrations. The optimized NCO nanosheet electrode exhibited a very high specific capacitance (2704 Fg^{-1} at 2 mA cm^{-2} in 3 M KOH) and low overpotential (315 mV at 10 mA cm^{-2} in 1 M KOH) with a Tafel slope of 59 mV dec^{-1}.

2. Experimental section

2.1. Synthesis

The NCO nanosheets were electrodeposited on the Ni foam in an aqueous bath containing different molar ratios of $Ni(NO_3)_2{\cdot}6H_2O$ and $Co(NO_3)_2{\cdot}6H_2O$ precursors. The schematic diagram of the NCO electrodeposition is presented in Fig. 1 (a)-(b). The synthesis pro- cess involves two steps: electrodeposition of mixed metal (Ni, Co) precursor, followed by a thermal annealing process. The Ni foam (1 x 5 cm^2) was cleaned by sonication in 3 M HCl, acetone, deionized water, and ethanol in order

to remove the oxide layer and surface impurities. In this procedure, the Ni foam is used as the working electrode; the graphite serves as the counter electrode; and the saturated calomel electrode (SCE) serves as the reference electrode. Thin films were obtained via potentiostatic electrode- position using a chronoamperometry technique. A constant deposition potential of -1.0 V (vs SCE) was maintained for 3 min at room temperature. The four different molar ratios (1:2, 1:1, 2:1, and 4:1) of $Ni(NO_3)_2{\cdot}6H_2O$ and $Co(NO_3)_2{\cdot}6H_2O$, were used to find an optimized NCO electrode film with the best electrocatalytic and elec- trochemical activities. The films that were deposited at 1:2, 1:1, 2:1, and 4:1 M ratios were denoted: NC_{12}, NC_{11}, NC_{21}, and NC_{41}, respectively. The pristine thin films were dried at 60 ^oC for 12 h in a vacuum oven, and then were annealed at 300 ^oC for 2 h with a ramping rate of 1 $^oC\ min^{-1}$ in a tube furnace.

2.2. Materials characterizations

The morphologies of the electrode films were investigated using field emission scanning electron microscopy (FESEM), a trans- mission electron microscope (TEM: JEOL 2010, JEOL, Japan) equipped with an energy-dispersive X-ray spectroscopy (EDS) accessory, and high-resolution transmission electron microscopy (HRTEM). The film crystallinity and chemical compositions were determined using X-ray diffraction (XRD) and X-ray photoelectron spectroscopy (XPS).

2.3. Electrochemical measurements

The electrochemical energy-storage and the OER electro- catalytic performance of the electrodes were evaluated via cyclic voltammetry (CV), galvanostatic charge-discharge (CD), linear sweep voltammetry (LSV), and electrochemical impedance spectroscopy (EIS) analyses. For the electrochemical measurements, a conventional three-electrode cell was used for which the NCO nanosheet electrode served as the working electrode, graphite served as the counter electrode, an SCE served as the reference electrode, and aqueous 3 M KOH solution was used as the electrolyte. For the OER catalytic measurements, the same three-electrode cell was used, where a platinum wire served as the counter electrode and 1 M KOH as the electrolyte. The electrode loading mass was determined by using a weight difference method, and it is about 0.3 mg/cm^2.

3. Results and discussion

Fig. 2 (a)-(b) shows the XRD patterns of the NCO electrodes. All of the samples show minor but noticeable diffraction peaks indicating their polycrystalline nature. The peaks observed at 19^o, 31^o, 37^o, and 66^o correspond to the (111), (220), (311), and (440) planes, respectively, of the spinel-$NiCo_2O_4$ crystalline structure (JCPDS No. 04-018-4105) [15,18]. The peaks from the Ni-foam substrate are marked with a star symbol. The broad feature at ~45^o may be due to the diffraction peak of the (311) plane. Compared with the Ni form peaks, the observed sample diffraction peaks are broad, indicating that the crystal size is small. Nonetheless, the absence of noticeable impurity peaks from the other crystal phases revealed that the Ni foam is uniformly covered by NCO.

Fig. 3(a)-(d) show electrode FESEM images, wherein a nano- sheet morphology with different nanosheet densities is apparent. With variation of the Ni-Co molar ratio, a progressive nanosheet-morphology evolution is observable. The nanosheets are aligned vertically and interconnected, producing a mesoporous structure. The thicknesses of the nanosheets are from 5 to 10 nm. This porous morphology could provide easy access for ions at the electrode/ electrolyte interface, short ion-transport pathways, and superior electron-collection efficiency [18]. Fig. 3 (e) shows the graph of the pore diameter versus the sample molar ratio.

The NCO nanosheets were further investigated using TEM and HRTEM analyses. Fig. 4 (a)-(b) shows the TEM and HRTEM images of the NC_{41} electrode, respectively. The lattice fringes of the NCO nanosheets are clearly observed in the HRTEM image. The observed lattice-distance "d" values of 0.21 nm and 0.25 nm correspond to the (400) and (311) planes, respectively, of the spinel $NiCo_2O_4$ [18]. The selected area diffraction (SAED) pattern exhibited diffuse rings, as shown in Fig. 4 (c), indicating that the sample was poly-crystalline. The inner diffuse rings were indexed to the (220), (111), and (311) planes, and these are consistent with the XRD results. Fig. 4 (d) shows the HRTEM element-mapping images of the NC_{41}, revealing the uniform distributions of the main constituent elements (Ni, Co, and O). These images show that the concentration of Ni is higher than those of Co and O. The compositional ratios obtained from the EDS analysis are presented in Fig. S1. As anticipated, the chemical compositions of all of the films are different; furthermore, also as expected, the NC_{41} sample shows a higher Ni content.

The elemental composition and oxidation states of the nickel cobaltite ($NiCo_2O_4$) are further confirmed using XPS data. Fig. 5 (a)e(d) shows the survey spectra and the core-level Ni-*2p*, Co-*2p*, and O-*1s* spectra, respectively, of the samples. In the XPS survey spectra in Fig. 5 (a), is a series of peaks that correspond to Ni, Co, O, and a small amount of carbon (C). The existence of C is because of surface contamination or environmentally adsorption. Fig. 5(b) shows the core-level Ni-2p spectra, wherein two main peaks Ni $2p_{1/2}$ (872.53 eV) and Ni $2p_{3/2}$ (853.26 eV) are observable. The major peak of Ni $2p_{3/2}$ and its satellite peaks (855.26 eV) are associated with Ni^{2+} and Ni^{3+} oxidation states [26]. As the Ni-precursor concentration was increased ($NC_{12} < NC_{11} < NC_{21} < NC_{41}$), the intensities of the Ni 2p1/2 and Ni 2p3/2 peaks also increased, but their peak positions remained almost unchanged. Fig. 5 (c) shows the core-level Co-*2p* spectra, wherein the two peaks Co $2p_{1/2}$ (795.03 eV) and Co $2p_{3/2}$ (781.07 eV) were detected. The main peak Co $2p_{3/2}$ and its satellite are associated with the Co2+ and Co3+ oxidation states [25]. Similarly, as the Co-precursor concentration was increased ($NC_{12} > NC_{11} > NC_{21} > NC_{41}$), the Co $2p_{1/2}$ (795.03 eV) and Co $2p_{3/2}$ (781.07 eV) peak intensities also increased. In the O-1s core spectra (Fig. 5 (d)), two peaks are observable (529.46 and 531.21 eV) that are ascribed to the metal-oxygen bond and a higher number of defect sites with low O coordination [15]. The XPS results revealed that the main composition of the films comprises the Ni^{2+} and Co^{2+} oxidation states, with coexistence of Ni^{3+} and Co^{3+} oxidation states. These results are in good agreement with those of the XRD analysis.

Fig. 6 (a) shows the CV curves of the electrodes, measured at 100 mV s^{-1} in a potential window of -0.1 to 0.45 V (vs SCE). For the sample with a higher Ni composition ($NC_{12} < NC_{11} < NC_{21} < NC_{41}$), its CV curve exhibits clear redox peaks with a larger area. These redox peaks originate from the Faradaic redox reaction between the metal oxide and metal hydroxide ($NiCo_2O_4 + OH^- + H_2O \leftrightarrow NiOOH + 2CoOOH +$ e-, $CoOOH + OH^-$ 4 $\leftrightarrow CoO_2 + H_2O + e^-$), and they are typical of pseudocapacitive behaviour. The superior CV performance of the NC_{41} electrode with the highest Ni concentration is presumably because its electrical conductivity is the most enhanced.

Fig. 6(b) shows the CD curves of the NCO nanosheet electrodes that were measured at 2 $mAcm^{-2}$. The nonlinear nature of the CD curves also revealed their pseudocapacitive behaviour and the faradaic

reaction occurring between the electrode and the electrolyte. The observed CD plateaus are consistent with the CV results. The absence of a sharp infrared drop during the discharge process suggests low internal resistance and the superior reversibility of the electrodes. The NC_{41} electrode shows a longer discharge time compared with the other three samples; obviously, this yielded a higher specific capacitance.

The specific capacitance (Cs) of the NCO-nanosheet electrodes was calculated from the CD curves using the following equation:

$$C_S = I\Delta t / m\Delta V \qquad (1)$$

where I is the applied current, Δt is the discharge time, m is the mass of the active material, and ΔV is the potential window. The calculated C_s values at 2 mA cm^{-2} for the NC_{41}, NC_{21}, NC_{11}, and NC_{12} are (2704, 2076, 1230, and 613) Fg^{-1}, respectively. The obtained C_s of 2704 Fg^{-1} is much higher than those of the binder-free Ni-foam/ N-CNT/$NiCo_2O_4$ NS (1472 Fg^{-1} measured at 1 Ag^{-1}) and of the Ni- foam-supported ultrathin mesoporous $NiCo_2O_4$ nanosheets (2010 Fg^{-1} measured at 2 Ag^{-1}), as can be seen in Table SI (Supporting Information) [15,18].

The C_S values of the electrodes that were measured at different current densities are presented in Fig. 6 (c). As the current density was increased, the Cs gradually decreased. For the NC41 sample, at its maximum capacitance of 2704 Fg^{-1} at 2 mA cm^{-2}, an 89.7% (2426 Fg-1) capacity was retained at a very high rate (20 mA cm^{-2}). For the other samples, the Cs values are more than (84, 85, and 89) % for NC_{12}, NC_{11}, and NC_{21}, respectively. The excellent rate performance of the NCO-nanosheet electrodes is attributed to their high surface area and improved electrical conductivity. The CV and CD-performance values of the NC41 sample at different scan rates are presented in Fig. S2 (a)-(b) of the Supporting Information. The linear increase of the cathodic current with respect to the scan rate that is shown in Fig. S2(a), indicates the pseudocapacitive nature and excellent reversibility of the electrode. These qualities are limited by a diffusion-controlled reaction at the electrode [27]. The CD characteristics of the NC41 sample at different current densities are shown in Fig. S2(b). As the current density was decreased, the discharge time became longer. The non-linear shape of the CD curve also confirms its pseudocapacitive nature, and the unchanged shape reveals the effective rate capability of the electrode.

The electrochemical cycling stability was investigated via CD measurements for 2000 cycles at the very high current density of 20 mAcm^{-2}. Fig. 6 (d) shows the measured capacitance as a function of the cycle-number plot for the samples. All of the samples show capacity retention of more than 80% even after long cycling. As the Co concentration was increased (NC_{41} / NC_{12}), the retention performance improved to as high as 89.2% for the NC_{12} sample, suggesting that Co contributes to the cycling stability. For the NC_{40} sample, which does not contain Co, the stability was dramatically decreased by 34%. The slightly smaller capacitance retention of NC_{11} compared with that of NC_{21} is probably due to the formation of different chemical states during 2000 charge-discharge cycles. The cycling stability for the NC_{41} and NC_{21} samples is extended up to 5000 cycles (see Supporting Information).

The electrochemical performances of the electrodes were evaluated by calculating the energy and power densities (Ragone plot). The energy density and the power density were derived as follows:

$$\text{Energy density } (E) = 0.5 \times C_{sp} \times \Delta V^2 \qquad (2)$$

Power density (P)= E/t (3)

where C_{sp}, ΔV, and t represent the specific capacitance, potential- voltage window, and discharge time, respectively. Fig. 7 shows the Ragone plot for the samples. The overall performance of the samples is excellent; the NC_{41} sample in particular, shows superior energy and power density compared with the other samples. A conventional two-electrode supercapacitor test for the NC_{41} sample is also carried out to check the feasibility of the electrode for real supercapacitor applications (see Supporting Information).

The electrocatalytic OER activities of the NCO-nanosheet electrodes were investigated using the linear sweep voltammetry (LSV) technique. The LSV curves were obtained using the standard three-electrode system in 1 M KOH electrolyte. The NCO-nanosheet electrodes were used as the working electrode, platinum wire served as the counter electrode, and a reversible hydrogen electrode (RHE) served as the reference electrode. The measured LSV curves of the electrodes are shown in Fig. 8. The applied-voltage range at a scan rate of 10 mV s^{-1} is between 1.0 and 1.75 V (vs. RHE). With increase of the Ni concentration (NC_{12} < NC_{11} < NC_{21} < NC_{41}), the LSV curve shifted toward a lower potential. An anodic peak is observed, and this is associated with the reversible reaction between the Ni^{2+} and Ni^{3+} [28,29]. The lowest overpotential of 315 mV at 10 mA cm^{-2} was obtained for the NC_{41} electrode, while the lowest overpotential of the bare Ni-foam substrate was ~470 mV.

The OER kinetics was evaluated using Tafel slope analysis. Fig. 8(b) shows the Tafel plot of the electrodes. The lowest Tafel slope of 59 mV dec-1 was obtained from the NC_{41} electrode. Fig. 8(c) shows the chronoamperometric curve of the NC_{41} electrode, which was measured at 0.53 V for 24 h. The NC_{41} sample retained a constant current of 9.45 mA cm^{-2} after the initial stabilization. The durability of the NC_{41} sample was evaluated at a constant potential of 0.53 V using the chronoamperometric method (vs. SCE).

To understand the observed superior electrochemical and electrocatalytic activities of the NC_{41} electrode, EIS and ECSA analyses were performed. Fig. 9(a) shows the EIS spectra of the nanosheet electrodes that were measured in the 1 M KOH electrolyte. The EIS curves display a semicircle in the high-frequency region and a straight line in the low-frequency region. These are associated with the charge-transfer resistance and diffusion of the OH^- ions, respectively (often referred to as the Warburg impedance). Notably, there is no semicircle at the NC_{41} and NC_{21} electrodes. The absence of a semicircle in the high-frequency region suggests that the charge transfer resistance (Rct) at the electrode and electrolyte interface is almost negligible. The EIS spectra were quantitatively simulated with the equivalent-circuit diagram, as shown in the inset of Fig. 9(a). The fitting parameters are presented in Table SII (Supporting Information). The charge-transfer resistance (Rct) of NC_{41} is the lowest among the samples, revealing that it has the most enhanced conductivity.

The accessible electrochemical-reaction surface area can be evaluated via ECSA analysis. The scan-rate-dependent CV curves $J_{dl}(\nu)$ in the linear-charging region were determined using the non- Faradaic specific capacitance of the double layer region C_{dl} (Fig. 9 (b)), as follows:

$$J_{dl}(\nu)=C_{dl} \times \nu \qquad (4)$$

The slope of the $J_{dl}(\nu)$ characteristics corresponds to the C_{dl}. The ECSA of the electrode was obtained using the following equation:

$$ECSA=C_{dl}/C_e \quad (5)$$

where C_e is the specific capacitance of the alkaline electrolyte used (0.04 mF/cm^{-2} for KOH). The calculated ECSA values of the NC_{12}, NC_{11}, NC_{21}, and NC_{41} are 307.5, 247.5, 285, and 385 cm^{-1}, respectively. The largest ECSA value of the NC_{41} electrode is consistent with its maximum specific capacitance and superior OER activity.

4. Conclusion

Mesoporous NCO nanosheet thin films were electrodeposited on Ni foam, and their bifunctional-electrochemical and oxygen- electrocatalytic activities were investigated. The bifunctionality of the nanosheet electrodes was optimized by changing of the ratio of the Ni and Co precursor concentrations during the electrodeposition. The XRD, TEM, and SAED analyses revealed that the nanosheet electrode is polycrystalline. The optimized NCO-nanosheet electrode shows a high specific capacitance of 2704 Fg^{-1} at 2 mA cm^{-2}, an excellent rate capability even at a high rate of 20 mA cm^{-2} (~90% retention), and excellent electrochemical stability over 2000 CD cycles. The optimized electrode also acted as a superior electro- catalyst for OER, showing an enhanced overpotential of 315 mV with a Tafel slope of 59 mV dec^{-1} at 10 mA cm^{-2}. The observed experimental findings revealed that Ni increases the number of electrochemical/electrocatalytic reaction sites and the conductivity, while Co enhances the electrochemical stability. The bifunctionality of the NCO nanosheets can be maximally enhanced by optimizing the Ni-Co compositional ratio. The present facile electrodeposition and characterization of NCO nanostructures might provide insights into the design and optimization of complex metal oxide and hydroxide-based bifunctional electrodes for electrochemical energy-storage and energy-conversion applications.

Acknowledgements

This work was supported by the National Research Foundation (NRF) of Korea (Grant Nos. 2015M2A2A6A02045252, 2015R1D1A1A01058851, 2015R1A2A2A01004782, 2016R1A6A1A03012877 and 2015R1D1A1A01060743).

References

[1] A.J. Esswein, D.G. Nocera, Hydrogen production by molecular photocatalysis, Chem. Rev. 107 (2007) 4022-4047.

[2] J. Wang, W. Cui, Q. Liu, Z. Xing, A.M. Asiri, X. Sun, Recent progress in cobalt- based heterogeneous catalysts for electrochemical water splitting, Adv. Mater. 28 (2016) 215-230.

[3] M.G. Walter, E.L. Warren, J.R. McKone, S.W. Boettcher, Q. Mi, E.A. Santori, N.S. Lewis, Solar water splitting cells, Chem. Rev. 110 (2010) 6446-6473.

[4] X. Kong, K. Xu, C. Zhang, J. Dai, S.N. Oliaee, L. Li, X. Zeng, C. Wu, Z. Peng, Free- standing two-dimensional Ru nanosheets with high activity toward water splitting, ACS Catal. 6 (2016) 1487-1492.

[5] H.F. Liang, F. Meng, M. Caban-Acevedo, L.S. Li, A. Forticaux, L.C. Xiu, Z.C. Wang, S. Jin, Hydrothermal continuous flow synthesis and exfoliation of NiCo layered double hydroxide nanosheets for enhanced oxygen evolution catalysts, Nano Lett. 15 (2015) 1421-1427.

[6] R.D.L. Smith, M.S. Prevot, R.D. Fagan, Z.P. Zhang, P.A. Sedach, M.K.J. Siu, S. Trudel, C.P. Berlinguette, Photochemical route for accessing amorphous metal oxide materials for water oxidation catalysis, Science 340 (2013) 60.

[7] H.Y. Jin, J. Wang, D.F. Su, Z.Z. Wei, Z.F. Pang, Y. Wang, Stabilization of silicon- carbon mixed oxides, J. Am. Chem. Soc. 137 (2015) 2688-2694.

[8] H. Wang, H.W. Lee, Y. Deng, Z. Lu, P.C. Hsu, Y. Liu, D. Lin, Y. Cui, Bifunctional non-noble metal oxide nanoparticle electrocatalysts through lithium-induced conversion for overall water splitting, Nat. Commun. 6 (2015) 7261.

[9] Fei Hu, Shengli Zhu, Shuangming Chen, Yu Li, Lu Ma, Tianpin Wu, Yan Zhang, Chengming Wang, Congcong Liu, Xianjin Yang, Li Song, Xiaowei Yang, Yujie Xiong, Amorphous metallic NiFeP: conductive bulk material achieving high activity for oxygen evolution reaction in both alkaline and acidic media, Adv. Mater. 29 (2017), 1606570.

[10] X.X. Zou, Y. Zhang, Noble metal-free hydrogen evolution catalysts for water splitting, Chem. Soc. Rev. 44 (2015) 5148-5180.

[11] L.C. Seitz, C.F. Dickens, K. Nishio, Y. Hikita, J. Montoya, A. Doyle, C. Kirk, A. Vojvodic, H.Y. Hwang, J.K. Norskov, T.F. Jaramillo, A highly active and stable IrOx/SrIrO3 catalyst for the oxygen evolution reaction, Science 353 (2016) 1011-1014.

[12] P. Chen, K. Xu, Z. Fang, Y. Tong, J. Wu, X. Lu, X. Peng, H. Ding, C. Wu, Y. Xie, Metallic Co4N porous nanowire arrays activated by surface oxidation as electrocatalysts for the oxygen evolution reaction, Angew. Chem. Int. Ed. 54 (2015) 14710.

[13] F. Song, X.L. Hu, Ultrathin cobalt-manganese layered double hydroxide is an efficient oxygen evolution catalyst, J. Am. Chem. Soc. 136 (2014) 16481-16484.

[14] F. Song, X.L. Hu, Exfoliation of layered double hydroxides for enhanced oxygen evolution catalysis, Nat. Commun. 5 (2014) 4477.

[15] H.F. Liang, F. Meng, M. Caban-Acevedo, L.S. Li, A. Forticaux, L.C. Xiu, Z.C. Wang, S. Jin, Hydrothermal continuous flow synthesis and exfoliation of NiCo layered double hydroxide nanosheets for enhanced oxygen evolution catalysis, Nano Lett. 15 (2015) 1421.

[16] Changzhou Yuan, Jiaoyang Li, Linrui Hou, Xiaogang Zhang, Laifa Shen, Xiong Wen (David) Lou, Ultrathin mesoporous NiCo2O4 nanosheets supported on Ni foam as advanced electrodes for supercapacitors, Adv. Funct. Mater. 22 (2012) 4592-4597.

[17] G.Q. Zhang, H.B. Wu, H.E. Hoster, M.B. Chan-Park, X.W. Lou, Controlled growth of NiCo2O4 nanorods and ultrathin nanosheets on carbon nanofibers for high- performance supercapacitors, Energy Environ. Sci. 5 (2012) 9453-9456.

[18] K.K. Lee, W.S. Chin, C.H. Sow, Cobalt-based compounds and composites as electrode materials for high-performance electrochemical capacitors, J. Mater. Chem. A 2 (2014) 17212-17248.

[19] Jian Wu, Pan Guo, Rui Mi, Xichuan Liu, Hui Zhang, Jun Mei, Hao Liu, Woon- Ming Lau, Li-Min Liu, Ultrathin NiCo2O4 nanosheets grown on three- dimensional interwoven nitrogen-doped carbon

nanotubes as binder-free electrodes for high-performance supercapacitor, J. Mater. Chem. A 3 (2015) 15331-15338.

[20] Yufei Zhang, Mingze Ma, Jun Yang, Haiquan Su, Wei Huang, Xiaochen Dong, Selective synthesis of hierarchical mesoporous spinel NiCo2O4 for high- performance supercapacitor, Nanoscale 6 (2014) 4303-4308.

[21] J.W. Xiao, S.H. Yang, Sequential crystallization of sea urchin-like bimetallic (Ni, Co) carbonate hydroxide and its morphology conserved conversion to porous NiCo2O4 spinel for pseudocapacitors, RSC Adv. 1 (2011) 588-595.

[22] J. Wang, K. Li, H.X. Zhong, D. Xu, Z.L. Wang, Z. Jiang, Z.J. Wu, X.B. Zhang, Synergistic effect between metal-nitrogen-carbon sheets and NiO nano- particles for enhanced electrochemical water-oxidation performance, Angew. Chem. Int. Ed. 54 (2015) 10530-10534.

[23] K.B. Xu, R.J. Zou, W.Y. Li, Q. Liu, X.J. Liu, L.J.Q. Hu, Design and synthesis of 3D interconnected mesoporous NiCo2O4@CoxNi1-x(OH)2 core-shell nanosheet arrays with large areal capacitance and high rate performance for super- capacitor, J. Mater. Chem. A 2 (2014) 10090-10097.

[24] L. Yu, G.Q. Zhang, C.Z. Yuan, X.W. Lou, Hierarchical NiCo2O4@MnO2 core-shell heterostructured nanowire arrays on Ni foam as high-performance super- capacitor electrodes, Chem. Commun. 49 (2013) 137-139.

[25] D.U. Lee, J.-Y. Choi, K. Feng, H.W. Park, Z. Chen, Electrodes: advanced extremely durable 3D bifunctional air electrodes for rechargeable zinc-air batteries, Adv. Energy Mater 4 (2014) 1301389.

[26] Seok-Hu Bae, Ji-Eun Kim, Hyacinthe Randriamahazaka, Song-Yi Moon, Jeong- Young Park, Il-Kwon Oh, Seamlessly conductive 3D nanoarchitecture of core- shell Ni-Co nanowire network for highly efficient oxygen evolution, Adv. Energy Mater 7 (2017), 1601492.

[27] Abu Talha Aqueel Ahmed, Harish S. Chavan, Yongcheol Jo, Sangeun Cho, Jongmin Kim, S.M. Pawar, Jayavant L. Gunjakar, Akbar I. Inamdar, Hyungsang Kim, Hyunsik Im, Facile route to NiO nanostructured electrode grown by oblique angle deposition technique for supercapacitor, J. Alloys Compd. 724 (2017) 744-751.

[28] Zhaoyang Wang, Jiantao Li, Xiaocong Tian, Xuanpeng Wang, Yang Yu, Kwadwo Asare Owusu, Liang He, Liqiang Mai, Porous nickel-iron selenide nanosheets as highly efficient electrocatalysts for oxygen evolution reaction, ACS Appl. Mater. Interfaces 8 (2016) 19386-19392.

[29] Yi Jia, Longzhou Zhang, Guoping Gao, Hua Chen, Bei Wang, Jizhi Zhou, Mun Teng Soo, Min Hong, Xuecheng Yan, Guangren Qian, Jin Zou, Aijun Du, Xiangdong Yao, A heterostructure coupling of exfoliated Ni-Fe hydroxide nanosheet and defective graphene as a bifunctional electrocatalyst for overall water splitting, Adv. Mater. 29 (2017), 1700017.

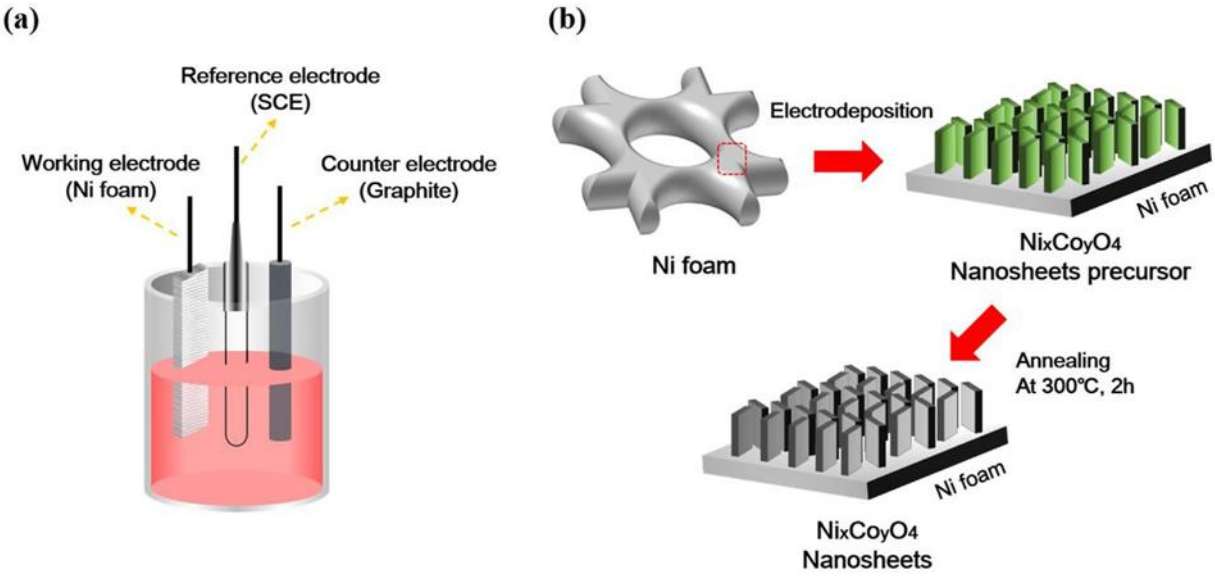

Fig. 1. Synthesis process of the nickel-cobalt oxide (NCO) nanosheet electrode: (a) typical electrodeposition schematic used for the preparation of a NCO nanosheet, and (b) schematic illustration showing the steps involved in the formation of a NCO nanosheet.

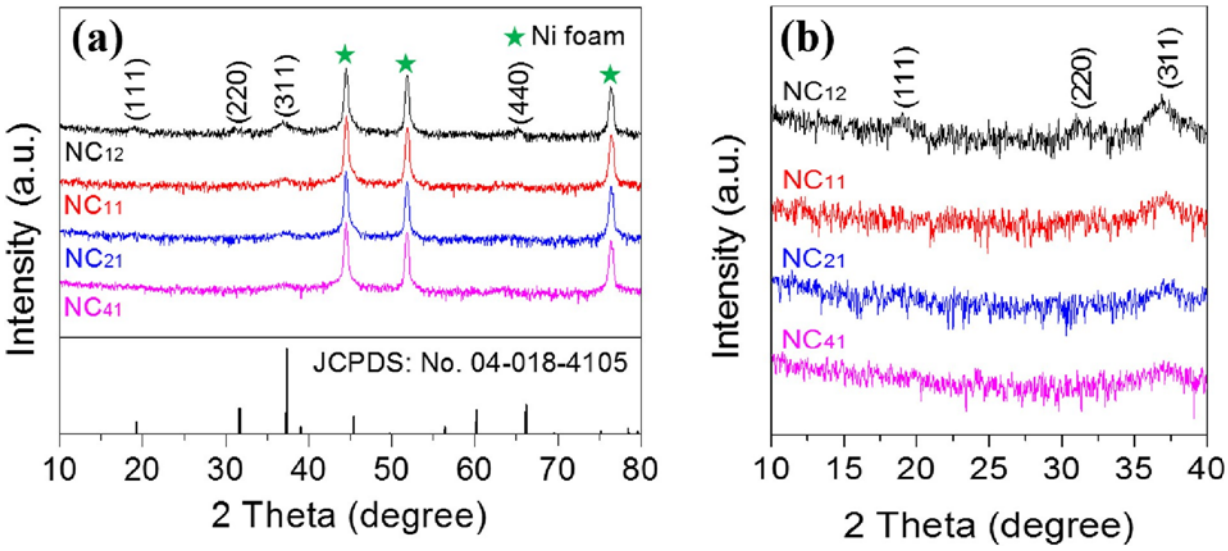

Fig. 2. (a) X-ray diffraction (XRD) spectra and (b) magnified X-ray diffraction (XRD) spectra of the nickel-cobalt oxide (NCO)-nanosheet electrodes synthesized at various nickel (Ni) to cobalt (Co) precursor concentration ratios.

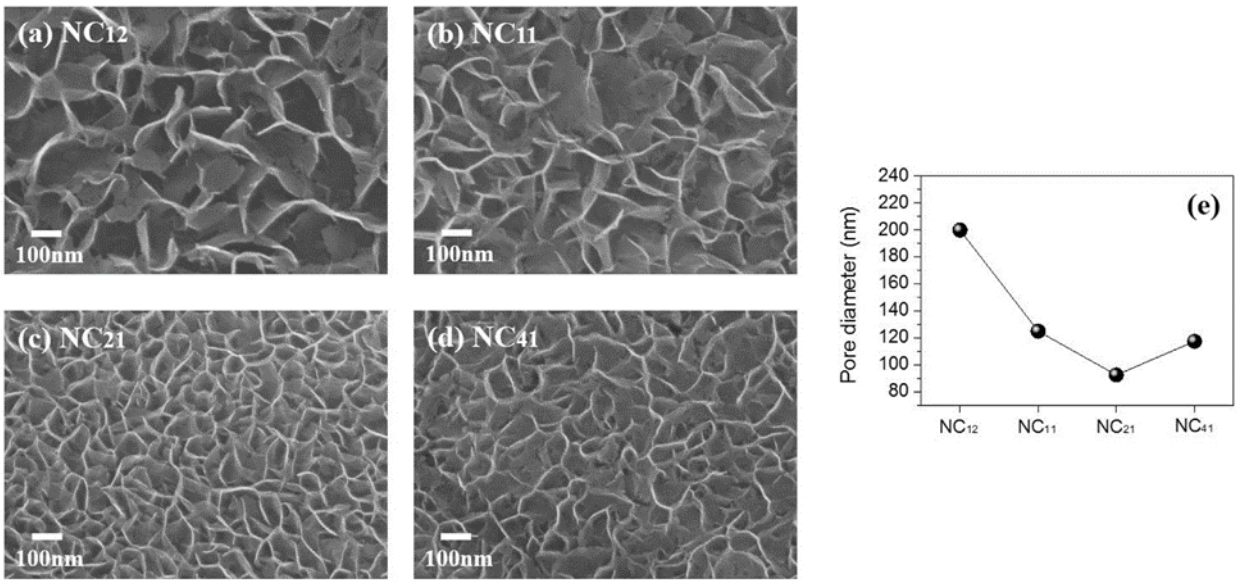

Fig. 3. Morphological characterization of the nickel-cobalt oxide (NCO)-nanosheet electrodes prepared at different nickel (Ni) to cobalt (Co) precursor concentration ratios: (a) NC_{12}, (b) NC_{11}, (c) NC_{21}, (d) NC_{41}, and (e) pore diameter vs sample molar ratio.

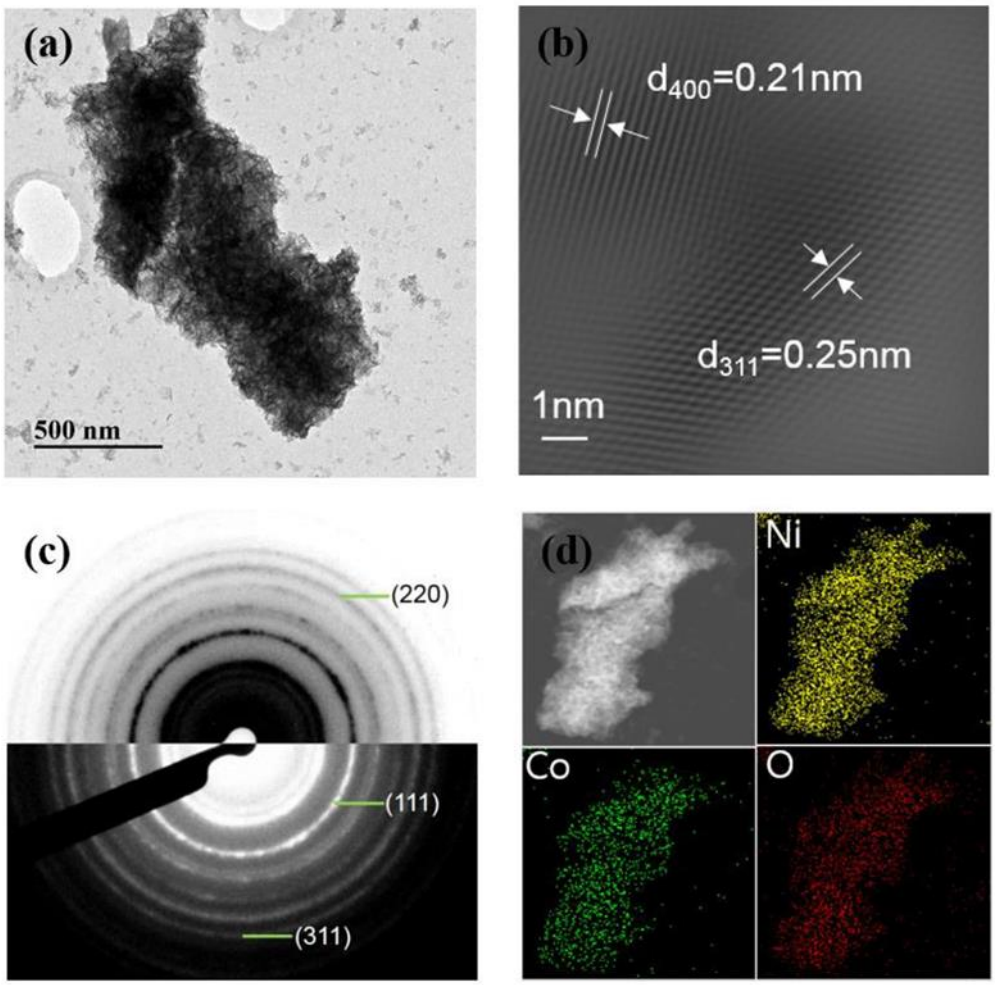

Fig. 4. (a) Transmission electron microscopic (TEM) and (b) High resolution transmission electron microscopic (HRTEM) characterization of the nickel-cobalt oxide (NCO)-nano- sheet electrode grown at the compositional ratio of NC_{41}; (c) Selective area electron diffraction (SAED) image and (d) Elemental-mapping images of nickel (Ni), cobalt (Co), and oxygen (O) confirm the existence of the stoichiometric composition of the electrode.

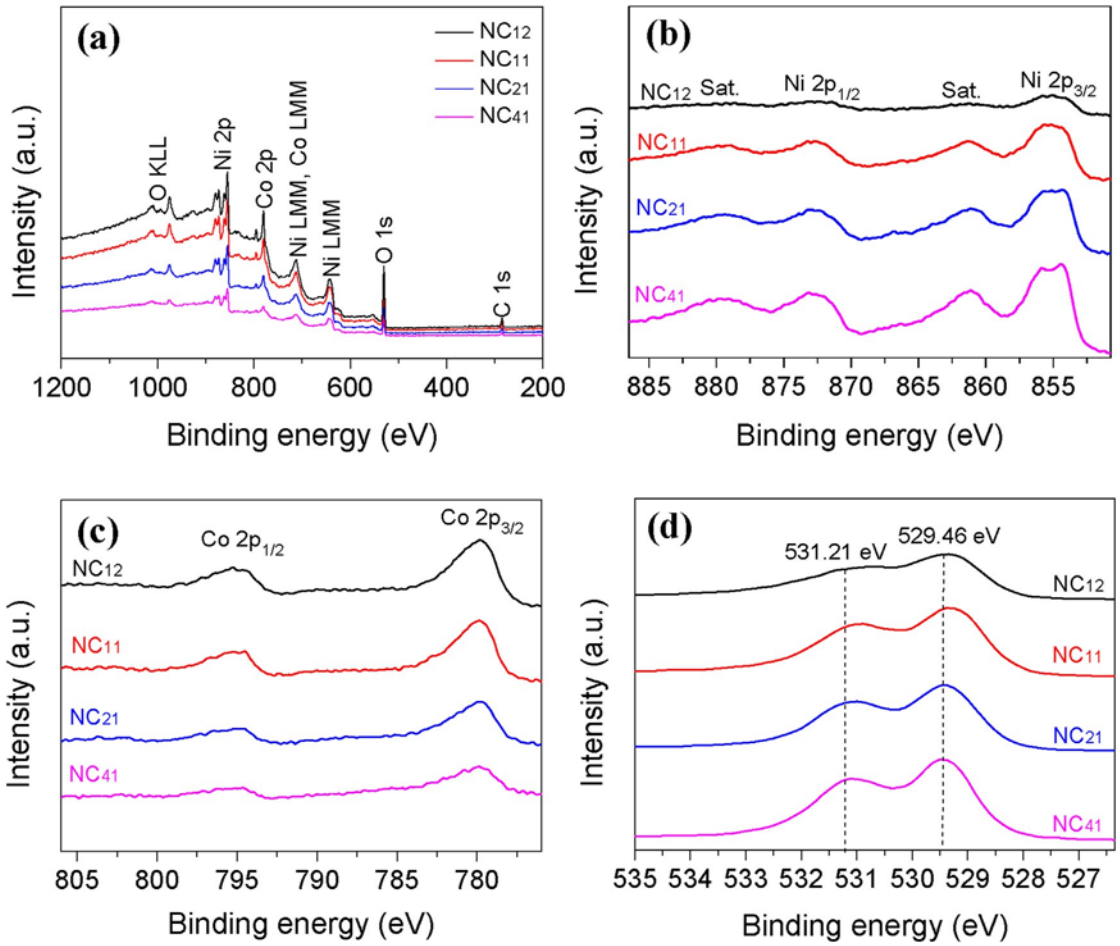

Fig. 5. X-ray photoelectron spectroscopy (XPS) characteristics of the nickel-cobalt oxide (NCO)-nanosheet electrodes prepared at the different nickel (Ni) to cobalt (Co) precursor concentration ratios of 1:2, 1:1, 2:1, and 4:1. (a) Survey spectra, (b) Core-level Ni-*2p* spectra, (c) Core level Co-*2p* spectra, and (d) Core level O-*1s* spectra.

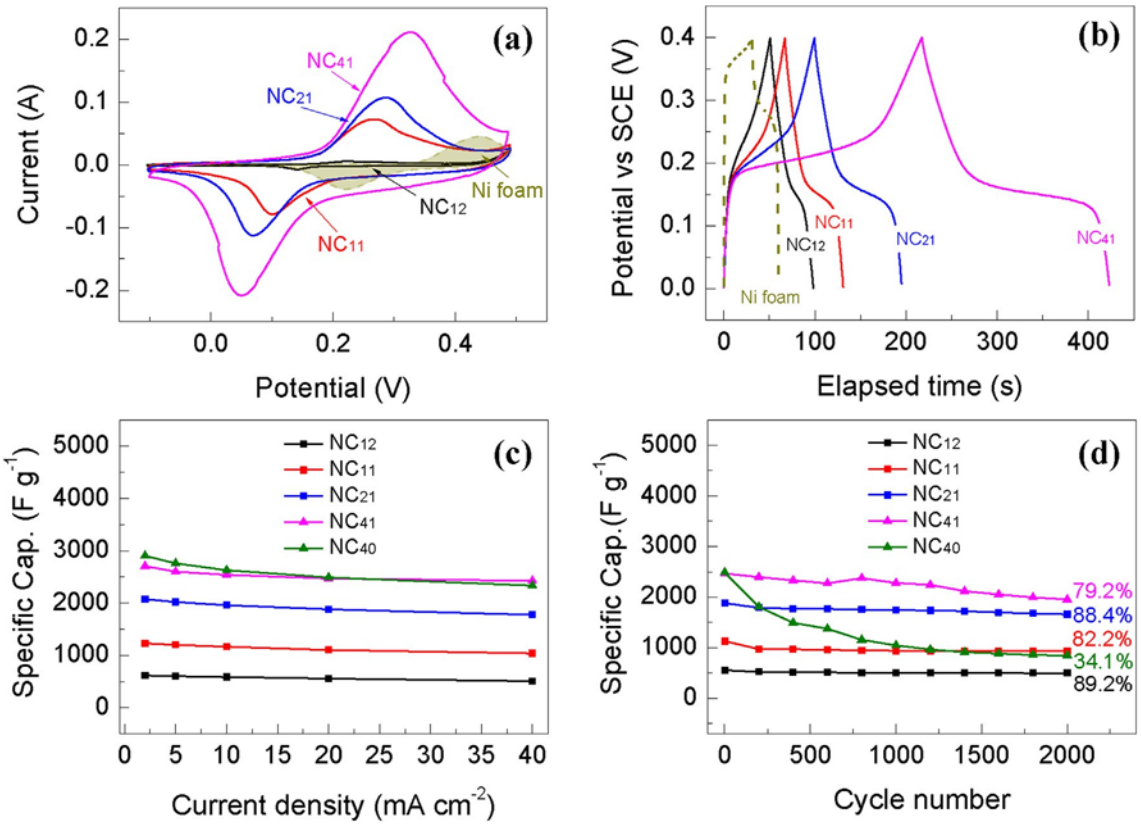

Fig. 6. Electrochemical properties of the nickel-cobalt oxide (NCO)-nanosheet electrodes: (a) Cyclic-voltammetry (CV) curves of the four different electrodes measured at a scan rate of 100 mVs^{-1}, (b) Galvanostatic charge/discharge (CD) characteristics of the NCO-nanosheet electrodes at the current density of 2 mA cm^{-2} in a potential range from 0 to 0.4 V, (c) Specific capacitance of all of the electrodes measured at the current densities of 2, 5, 10, 20, 40 $mAcm^{-2}$, and (d) Electrochemical cycling stability over 2000 CD cycles at the current density of 20 $mAcm^{-2}$.

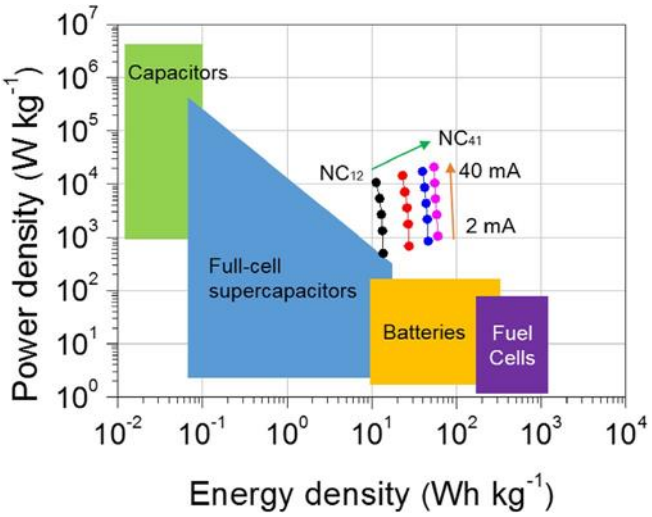

Fig. 7. Ragone plot showing energy density in relation to the power density of the samples.

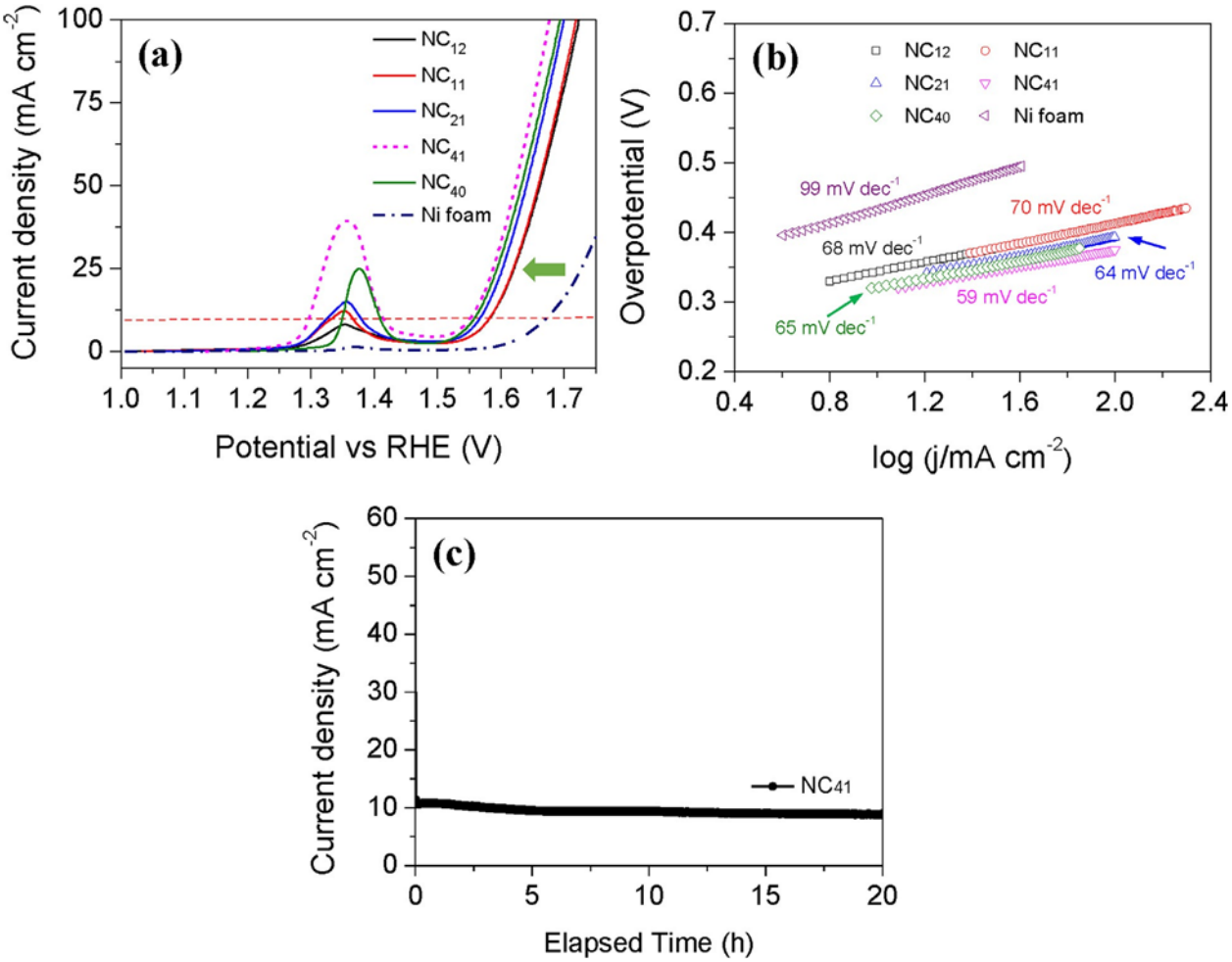

Fig. 8. Electrocatalytic properties of the nickel-cobalt oxide (NCO)-nanosheet electrodes: (a) Linear sweep voltammetry (LSV) plots that were obtained using the standard three- electrode system in 1 M KOH electrolyte, (b) Tafel plots that were obtained with all four of the electrodes, and (c) Chronoamperometric testing of the NCO nanosheet electrodes for 20 h in 1 M KOH electrolyte.

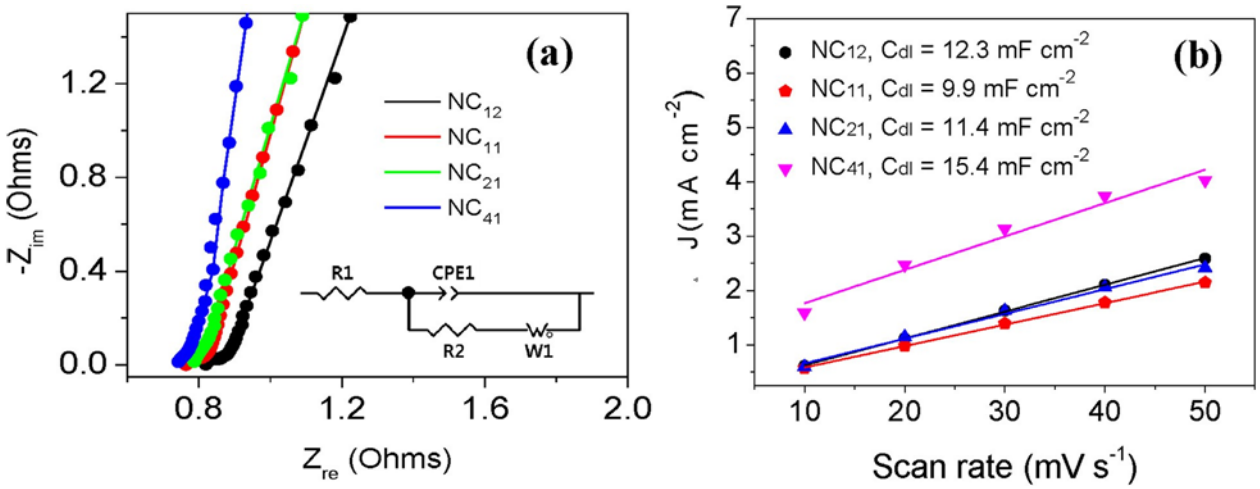

Fig. 9. (a) Electrochemical impedance spectroscopy (EIS) spectra of the nanosheet electrodes and (b) double-layer capacitance (C_{dl}) obtained from the cyclic-voltammetry (CV) curves as a function of scan rate (mVs^{-1}).